Check for updates

A green carbon dot@silver nanoparticle hybrid: as a turn-on fluorescent probe for the detection and quantification of cholesterol and glucose†

Nasrin Rahmatian,[a] Shahryar Abbasi,*[a] Naser Abbasi[b,c] and Mohammad Tavakkoli Yaraki ✪ *[d]

Cholesterol and glucose are two important biomarkers that are linked to different human diseases. In this work, we have designed a turn-on fluorescent biosensor based on carbon dots hybridized by AgNPs (CD@AgNPs). *Oliveria decumbens* Vent. extract was used as a rich carbon source for the green synthesis of carbon dots, which exhibited excitation-dependent fluorescence with maximum emission at 409 nm under 350 nm excitation. In this approach, hydrogen peroxide, a by-product of enzymatic reactions between oxidase enzymes and analytes, etches AgNPs, leading to fluorescence recovery. The designed biosensor showed a great linear range (2–60 μM for cholesterol and 4–250 μM for glucose) with very low limits of detection (3 μM for cholesterol and 38 μM for glucose), which are lower than the concentrations of these biomarkers in human body fluids. The great selectivity and sensitivity of the designed biosensor enable it to be used for the detection of biomarkers in complex media such as artificial human plasma in only 30 min. This work could open new avenues for researchers in the fields of sustainability and biomedicine, where green and accurate biosensors are required.

1. Introduction

Cholesterol is a major component of cell membranes, and it is a critical precursor for the synthesis of steroid hormones. However, elevated serum cholesterol levels are implicated in atherosclerosis and other coronary artery diseases.[1] Unlike triglyceride metabolism, the human body does not have any enzymes to metabolize cholesterol into energy.[2] As a result, excessive absorption of cholesterol in the diet may increase the concentration of cholesterol in the blood, which leads to the occurrence of cholesterol-related diseases. Therefore, determining the amount of cholesterol in the diet and human serum is of great importance in the food industry and health sectors.[3–5]

Insulin hormone is the main regulator of carbohydrate metabolism and also prevents the breakdown of fat into fatty acids (lipolysis) in the body. Insulin resistance is when cells respond less to this process, resulting in increased blood sugar, which is why it is considered a reason for diabetes, pre-diabetes, and type 2 diabetes.[6] Fats also break down quickly in the body and cause disturbances in the level of cholesterol. According to the mentioned points, developing sensitive diagnostic methods for the detection of cholesterol and glucose in body fluids is necessary to avoid false positive and negative results that threaten public health all over the world.[7]

The standard reference method for the measurement of cholesterol is a multi-step technique based on the modified Abell–Kendall method,[8] which provides approximately accurate results with minimum errors within 24 to 72 hours after receiving the sample.[9] However, this method is tedious and requires relatively complex technical facilities and skills.[10,11] In the last two decades, biosensors based on various techniques such as surface plasmon resonance,[12] electrochemical methods,[13] chromatography,[14] field effect transistors[15] and enzymatic methods such as enzyme cascade system sensors[16] and catalytic nanozymes[17] have been developed. Although these methods effectively identify cholesterol and glucose in complex samples, the need for expensive equipment and complex sample pretreatments has limited their use in diagnostic laboratories. Among the optical biosensors, turn-on

aDepartment of Chemistry, University of Ilam, Ilam, Iran.
E-mail: Sh_abbasi@ilam.ac.ir
bDepartment of Pharmacology, School of Medicine, Ilam University of Medical Sciences, Iran
cBiotechnology and Medicinal Plants Research Center, Ilam University of Medical Sciences, Ilam, Iran
dSchool of Natural Sciences, Faculty of Science and Engineering, Macquarie University, NSW 2109, Australia. E-mail: mohammad.tavakkoliyaraki@mq.edu.au, mty206@yahoo.com
†Electronic supplementary information (ESI) available. See DOI: https://doi.org/10.1039/d5nr00629e

fluorescent probes have found their applications in different biomedical applications, owing to their high sensitivity and selectivity.[18,19] Owing to the high selectivity of enzymes and the high sensitivity of fluorescent probes, designing bio-sensors based on the combination of these two approaches could open new avenues for researchers in the biomedical field.

Silver nanostructures are well known for their fluorescence quenching ability due to energy transfer from excited fluorophore molecules to silver nanostructures.[20,21] Cholesterol oxidase (ChOx) and glucose oxidase (GOx) enzymes could oxidize cholesterol and glucose molecules, respectively, and produce hydrogen peroxide. The produced hydrogen peroxide could etch the silver,[22] and therefore, using a fluorophore/metal hybrid nanostructure in designing biosensors could be an interesting approach for designing turn-on fluorescent probes for the detection of cholesterol and glucose.

Carbon dots (CDs), with a size of less than 5 nm, are quasi-spherical nanoparticles with 1 to 4 layers of graphene in the core and rich surface functional groups such as hydroxyl, epoxy, and carboxyl. They are a new class of carbon nano-materials that have unique optical properties such as wavelength-dependent fluorescence, high solubility in water, low toxicity, and excellent thermal and optical stability.[23,24] CDs could be synthesized from any carbonic sources,[25] making them ideal nanomaterials that could play an important role in the circular economy *via* green and environmentally friendly synthesis approaches.[26,27] While different plant extracts have been used for the synthesis of carbon dots, investigation of the potential of new plant extracts for the synthesis of carbon dots is still of interest since plant extracts are enriched with different bioactive molecules, which could give unique properties to the carbon dots.

Lal Kohestan plant with the scientific name of *Oliveria decumbens* Vent. from the *Apiaceae* family is a native plant of *Flora Iranica* and southwestern Iran in the Zagros mountains. The aerial parts of this plant are used in traditional medicine to treat indigestion, diarrhea, abdominal pain and fever. The two main compounds in the extract of this plant are thymol (47.06%) and carvacrol (23.31%),[28] while it also contains γ-terpinene and *p*-cymen.[29] To the best of our knowledge, there is no report on the green synthesis of carbon dots from the extract of this plant.

In this research, we have developed a green microwave-based synthesis route for converting *Oliveria decumbens* Vent. plant extract as a carbon source to carbon dots. Then, we have made CD@AgNP hybrid nanostructures by directly reducing the Ag$^+$ ions on the surface of CDs. The as-synthesized CD@AgNP hybrid nanostructure with quenched fluorescence was used as a probe to detect and quantify cholesterol and glucose in the presence of cholesterol oxidase and glucose oxidase enzymes, respectively. The designed biosensor could not only be used for the quantification of the two studied analytes but could also be used as a naked-eye colorimetric assay for detection purposes. The high selectivity and sensitivity of this biosensor indicate that it is a promising candidate to replace other biosensors for cholesterol and glucose detection in complex biological samples.

2. Chemicals and experimental

2.1. Chemicals

Oliveria decumbens Vent. plant was gathered from the Zagros mountains in southwestern Iran. Glucose, cholesterol, silver nitrate (AgNO$_3$), acetate buffer (AB), and 3-(*N*-morpholino) propane sulfonic acid buffer (MOPS) were purchased from Sigma-Aldrich (Saint Louis, USA). Glucose oxidase was purchased from Sinopharm Chemical Reagent Co. Ltd (Shanghai, China). Cholesterol oxidase was purchased from Shanghai Sangon Biotechnology Co., Ltd. Artificial human plasma fluid (BZ273) was obtained from BioChemazone, USA. Tris buffer and phosphate buffered saline (PBS) were obtained from Merck (Darmstadt, Germany). All solutions were prepared using Milli-Q deionized water (18.2 MΩ cm).

2.2. Synthesis of CDs from the plant extract

Lal Kohistan plant (scientific name: *Oliveria decumbens* Vent.) was collected from the Zagros mountains in Southwest of Iran. The plant extract was collected by the Soxhlet method in a methanol : water solvent with a volume ratio of 3 : 1 (120 mL in total) for 16 hours. The extract was filtered through Whatman no. 1 paper. Then, the filtered extract was used as a green source of carbon for the synthesis of carbon dots. 50 mL of the extract was placed in a microwave (700 W) for 10 min. The color of the extract solution changed from green to brown, and the resulting solution was centrifuged (15 000 rpm) for 20 min. After separation of the supernatant, it was passed through a 0.22 μm syringe microfilter to remove the larger particles. The brown carbon dots were stored in a dark container at a temperature of 4 °C in a refrigerator for further analysis.

2.3. Synthesis of a carbon dot–silver nanoparticle (CD@AgNP) hybrid nanostructure

40 mL of CD solution (60 μg mL^{-1}) was added (dropwise) to 10 mL of AgNO$_3$ solution (20 mM). The mixture was incubated for 30 minutes until the color of the solution changed from light yellow to light brown.

2.4. Identification of hydrogen peroxide (H$_2$O$_2$), cholesterol (Cho) and glucose (Glu) in buffer

2.4.1. Detection of hydrogen peroxide. In order to detect hydrogen peroxide (H$_2$O$_2$), 500 μL of hydrogen peroxide solution (different concentrations) and 500 μL of CD@AgNPs in 5 mM phosphate buffered saline (PBS, pH = 7.3, equivalent to the physiological pH of the body) were mixed and incubated for 30 minutes at 37 °C. Then, the spectrum was recorded for each sample.

2.4.2. Detection of cholesterol. Identification of cholesterol (Cho) in phosphate buffered saline (PBS, 5 mM at pH = 7.3) was performed in two steps. In the first step, a mixture (500 μL) of cholesterol oxidase (ChOx, 1 mg mL^{-1} final concen-

tration) and cholesterol (different concentrations) was incubated for 30 minutes at 37 °C. The amount of produced H_2O_2 is directly proportional to the amount of cholesterol concentration in the solution. In the second step, 500 µL of CD@AgNPs (2× diluted) was added to the reaction solution and incubated again for 30 minutes at 37 °C. Finally, the fluorescence emission was measured for different concentrations of cholesterol.

2.4.3. Detection of glucose. Similar to the detection of cholesterol, the same amounts of glucose and glucose oxidase (GOx) were used for the detection of glucose. Finally, the fluorescence emission was measured for different concentrations of glucose.

2.5. Identification of glucose and cholesterol in complex media

The artificial human plasma sample was diluted 50 times with phosphate buffer (PB, 5 mM, pH = 7.3), and ChOx (1 mg mL⁻¹ final concentration) and cholesterol (20 µM final concentration) were added to the plasma, followed by incubation for 30 minutes at 37 °C to produce H_2O_2. In the next step, 500 µL of 2× diluted CD@AgNPs was added to 500 µL of the previous solution and was incubated at 37 °C for 30 min. Finally, the fluorescence emission was recorded.

Similarly, a negative control sample was prepared by adding GOx (1 mg mL⁻¹ final concentration) and glucose (200 µM final concentration) to 50× diluted plasma, followed by incubation for 30 minutes at 37 °C. Then, 500 µL of CD@AgNPs was added to 500 µL of the prepared solution, followed by incubation at 37 °C for 30 min. Finally, the fluorescence emission was recorded for each sample.

2.6. Instrumentation

Fluorescence spectra were recorded using a Shimadzu RF-5301PC fluorescence spectrophotometer (1 cm quartz cell) at 25 °C. UV-Vis absorbance spectra were recorded using an Agilent Carry 60 UV-Vis spectrophotometer (USA) with a 10 mm path length quartz cell. Fourier transform infrared (FT-IR) spectra were recorded in KBr pellets on a Shimadzu IR470 spectrometer. TEM images of the synthesized nanomaterials were recorded using a H600 TEM (Hitachi, Japan). The X-ray diffraction pattern of CD and CD@AgNPs was recorded on an AXS-D8 X-ray diffractometer (Bruker, Germany). The particle size was determined by dynamic light scattering and the ζ-potential was determined by electrophoretic light scattering on the particle size and zeta-potential analyzer, Zetasizer Nano, Malvern Instruments Ltd, UK. Centrifugation was performed using a HERMLEZ 36 HK apparatus (Wehingen, Germany).

3. Results and discussion

3.1. Synthesis and characterization of CDs

Fig. 1a shows the step-by-step synthesis procedure for preparing CDs from *Oliveria decumbens* Vent. extract *via* a microwave-assisted synthesis method. *Oliveria decumbens* Vent. extract is rich in aromatic and medicinal compounds such as octacosane, carvacrol, thymol, stigmasterol, kaempferol-3-O-(6″-O-trans-coumaryl) glucoside (tiliroside), kaempferol-3-O-(6″-O-trans-coumaryl) glucoside, and 3-hydroxythymol-6-O-D-glucopyranoside (Fig. S1a†).[26] These monoterpene phenolic compounds contain heteroatoms which are an excellent precursor of carbon and heteroatoms in the synthesis of carbon dots. Generally, molecules containing S and N could improve the quantum yield of CDs.[27] The presence of different surface groups creates different energy states, which consequently results in the emission from different energy states, and in turn, excitation-dependent emission. On the other hand, the presence of amine and sulphur-based groups, which naturally exist in most of the extract, eliminates non-radiative electron trapping by removing other functional groups and stabilizing the surface energy trap, leading to a larger energy gap and therefore, blue-green emission.[28,29] The as-synthesized CDs showed bright blue-green fluorescence when exposed to UV light at 365 nm (Fig. 1b). The fluorescence spectrum was investigated with a gradual increase in excitation wavelength (λ_{ex}) from 300 nm to 490 nm, where excitation wavelength-dependent fluorescence emission was observed. In particular, the maximum fluorescence emission was observed at a peak centered at λ_{em} = 409 nm when the excitation wavelength was 350 nm. This wavelength-dependent fluorescence is a typical behavior in most of the CDs, which is due to the different electron transitions in the core and surface states in CDs.[30] The UV-visible spectrum of the CD had peaks in the high-energy region of 200 nm to 350 nm. The peak at 257 nm is attributed to the π–π* transitions in C=C and C=N bonds and the peak at 210 nm originates from the n–π* transitions in CD.[31,32] The size and morphology of the as-synthesized CDs were investigated by dynamic light scattering (DLS) and transmission electron microscopy. The hydrodynamic size distribution is in good agreement with the average size obtained by TEM (3 nm), where the CDs were monodisperse with a quasi-spherical shape (Fig. S1b and c†).

3.2. Synthesis and characterization of CD@AgNPs

Fig. 2a is a schematic illustration for the synthesis of the CD@AgNP hybrid. As can be seen, the electrostatic interaction between the surface functional groups (*i.e.*, oxygen functional groups such as carboxyl and hydroxyl) on CDs and Ag⁺ ions is necessary in order to prepare the CD@AgNP hybrid system. When CDs with enriched surface functional groups are mixed with positively charged silver ions (Ag⁺), the weak intermolecular van der Waals force affects the CDs, leading to the oscillation of the electron cloud and the formation of temporary dipoles.[33] This enables the carboxyl groups on the surface of CDs to interact with Ag⁺ ions through electrostatic interactions and reduce them, and in turn, the formation of a hybrid system.[34] The formation of homogeneous hybrid CD@AgNPs was examined by centrifugation of the final solution at 10 000 rpm for 10 minutes, where no precipitation was obtained, indicating the formation of a hybrid system with
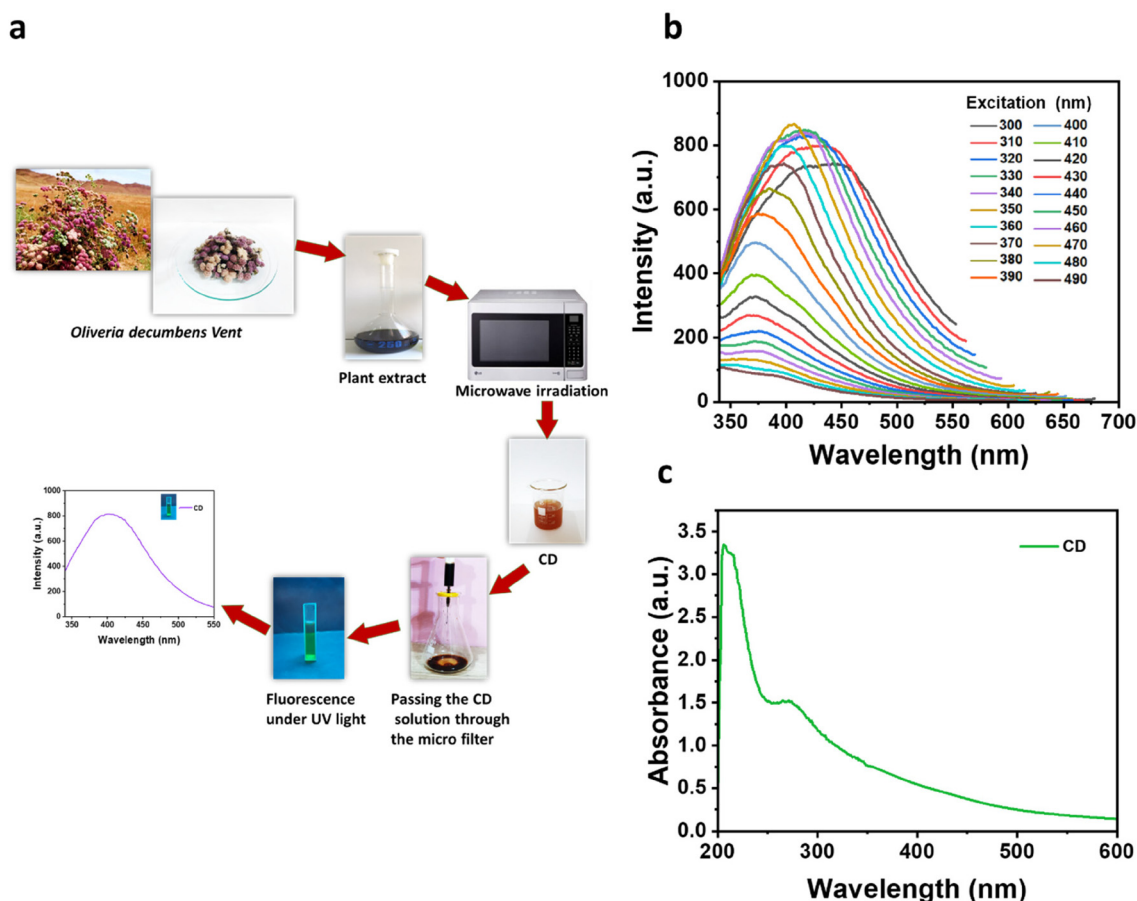
Fig. 1 (a) Schematic illustration of the green synthesis of carbon dots from *Oliveria decumbens* Vent. extract as a precursor, (b) excitation wavelength–dependent fluorescence spectra and (c) the absorption spectrum of the as-synthesized carbon dots.

high stability. To investigate whether there is a CD@AgNP hybrid or a mixture of AgNPs and CDs, we have synthesized citrate-capped silver nanoparticles of similar size (evidenced by a similar LSPR peak position in Fig. 2b) and a mixture of these citrate-capped AgNPs (negatively charged) and CDs was prepared. This thin-layer coating creates a distance that extends and modulates the electrostatic interactions and the quenching effect by the FRET mechanism and the formation of the CD@AgNP hybrid. On the other hand, citrate-capped silver nanoparticles have negative charges around them and due to the surface functional groups of CDs and the negative charge, the repulsive interaction is more dominant.[35,36] As can be seen in Fig. 2b, the UV-visible spectrum of CD@AgNPs had a peak at 414 nm (for AgNPs grown by reduction on CDs) and two other peaks at 259 nm and 220 nm, which are related to CDs. However, pure CDs had two peaks at 257 nm (π–π* transition) and 210 nm (n–π* transition). The observed red shift in the position of peaks in the UV-visible spectrum of CD@AgNPs could be due to the hybridization between CDs and AgNPs. Additionally, the fluorescence quenching efficiency was 36% for the mixture of CDs and citrate-capped AgNPs with a similar size and LSPR peak, while it was 94% for CD@AgNPs due to complete charge transfer (through FRET:

fluorescence resonance energy transfer) between CDs and AgNPs in the CD@AgNPs (Fig. 2c).[37,38]

On the other hand, the emission spectrum of CDs (showing an emission maximum at 409 nm) and the absorption spectrum of AgNPs in the CD@AgNP nanohybrid (absorption maximum at 414 nm) show a significant spectral overlap. This spectral overlap provides the necessary conditions for fluorescence resonance energy transfer (FRET), during which an excited donor (CD) transfers energy to an acceptor group (AgNP) through a non-radiative process, leading to fluorescence quenching in the emission spectrum of the CD@AgNP nanohybrid.[39,40]

The TEM image shows the heterogeneous structure of CD@AgNPs with uniform dispersion and low apparent aggregation where AgNPs with a spherical shape (15 ± 1 nm) have been formed (Fig. 2d). Fig. S2a and b† show the UV-visible spectrum for CD@AgNPs and CDs. The UV-visible spectrum of CDs shows a broad shoulder at 257 nm and a sharp peak at 210 nm, which are attributed to the successive transitions in the C=C ring and C=O functional groups on the surface of CDs. The spectrum of CD@AgNPs shows a peak at 414 nm due to the presence of AgNPs in the solution, followed by peaks at 259 nm and 220 nm, which confirms the presence of CDs in
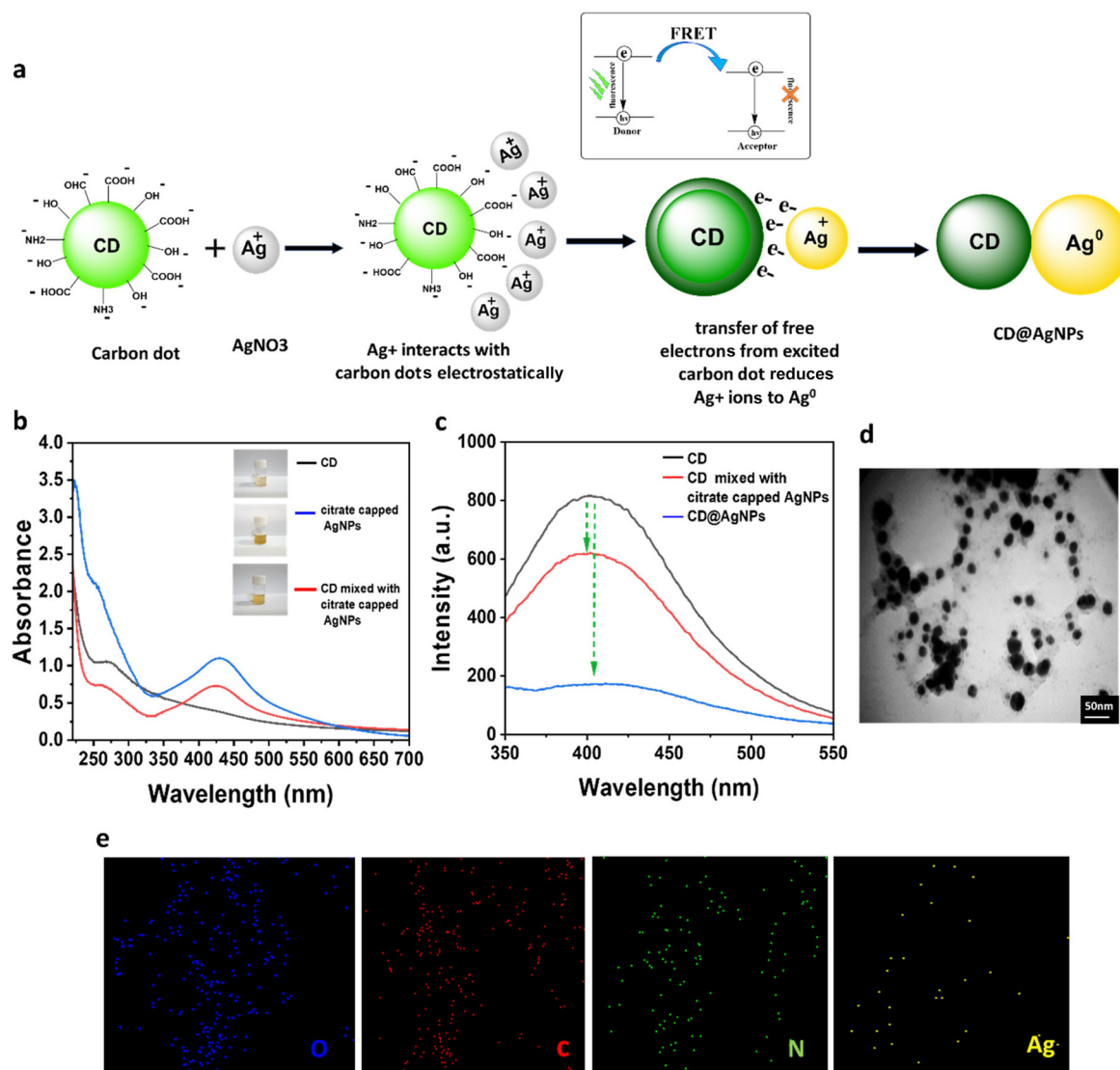
Fig. 2 (a) Schematic illustration of the formation of the CD@AgNP hybrid. (b) UV-visible spectrum of CDs, AgNPs with citrate coating, a mixture of CDs with citrate-coated AgNPs, and the CD@AgNP hybrid. (c) Fluorescence emission spectrum of CDs, the mixture of CDs with citrate-coated AgNPs and the CD@AgNP hybrid. (d) TEM images of CD@AgNPs. (e) EDX image of the dispersion of each of the elements constituting CD@AgNPs: O element, C element, N element, and Ag element.

CD@AgNPs.[33,41] The CD solution under sunlight has very bright yellow color, and the colloidal solution of CD@AgNPs has brownish yellow color. Such a color change and the lack of observation of fluorescence in CD@AgNPs under 365 nm irradiation further confirm the presence of AgNPs in the vicinity of CDs.

We further characterized the as-synthesized CD@AgNP hybrid using different techniques. Zeta potential (ζ-potential) data obtained from different samples of CDs and CD@AgNPs are shown in Fig. S2c†. The synthesized CDs had a zeta potential of -3.07 ± 0.24 mV, which strongly indicates the presence of various functional groups on the surface of CDs. The zeta potential value for the CD@AgNP hybrid was 30.13 ± 4.15 mV, indicating the effect of AgNPs and its surface charge on the zeta potential value of the hybrid.

Energy dispersive X-ray spectroscopy (EDX) was performed to evaluate the composition percentage of the elements and the purity of the synthesized nanomaterials in the prepared samples. The EDX of the green synthesized CDs and CD@AgNPs obtained from different peak areas of Ag, C, N, and O in the range of 1–4 keV is shown in Fig. S2d and e.† The findings confirm the formation of AgNPs in the CD@AgNP hybrid. The images of the dispersion of each of the elements in CD@AgNPs are shown in Fig. 2e.

X-ray photon spectroscopy (XPS) analysis was used to further determine the chemical structure and bond connections in the CD@AgNP hybrid and CDs. As shown in Fig. 3a, CD@AgNPs have the same chemical structure as CDs except for a series of peaks related to silver. Comprehensive analysis of the XPS spectrum of CDs revealed the presence of C(1s),
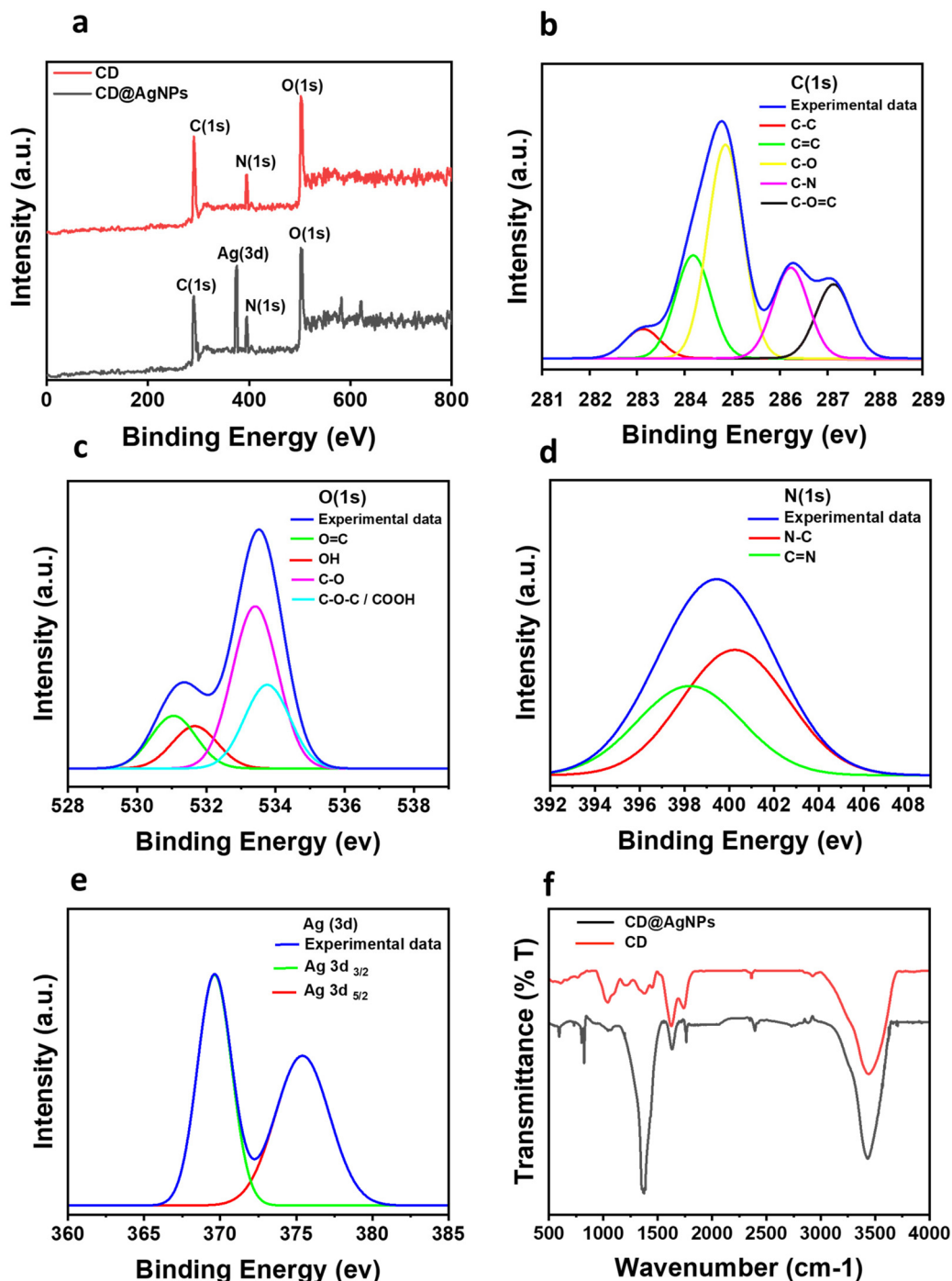
Fig. 3 Analysis of the structural characteristics of CDs and the CD@AgNP hybrid prepared by the green synthesis method. (a) Full XPS spectrum of CDs and the CD@AgNP hybrid, (b) C 1s photoelectron spectrum, (c) XPS spectrum of the N 1s peak, (d) O 1s XPS spectrum, (e) XPS spectrum of the Ag 3d peak, and (f) FTIR spectra of the synthesized CDs and CD@AgNPs.

O(1s) and N(1s) elements on the surface, which are three strong peaks at 287.22 eV, 504.16 eV, and 397.01 eV, respectively. The CD@AgNP hybrid has a similar chemical structure to CDs except for a series of silver peaks at 376.51 eV.

The surface spectrum of the C(1s) nucleus shows five peaks (Fig. 3b). The peaks related to the bonding connections (C=C) and (C–C) at 283.12 eV and 284.43 eV, respectively, are related

to the presence of graphite sp^2/sp^3 hybrid structures.[42] The peaks at 284.38 eV, 286.10 eV, and 287.22 eV confirm the presence of (C–O=C), (C–N), and (C–O) bonds in the structure of the CD@AgNP hybrid, respectively. Fig. 3c shows the presence of O 1s atoms in four bond structures C=O, O–H, C–O, and C–O–C at 531.14 eV, 531.64 eV, 533.23 eV, and 533.70 eV, respectively. In Fig. 3d, the deconvolution spectrum of the N 1s level

shows two peaks at 398.10 eV and 400.31 eV, which can be assigned to C=N and C–N, respectively. Additionally, the XPS profile in Fig. 3e includes Ag $3d_{5/2}$ and Ag $3d_{3/2}$ peaks at 368.32 eV and 375.22 eV, respectively, which show the unique splitting of the Ag 3d doublet, which corresponds to the metallic state of Ag^0 as a result of the reduction of $AgNO_3$.[43]

Furthermore, the results of Fourier transform infrared spectroscopy (FTIR) (Fig. 3f) support the XPS data obtained for CDs and the CD@AgNP hybrid. The FTIR spectrum of the green CDs synthesized using *Oliveria decumbens* Vent. plant extract by microwave radiation shows the presence of broad and strong peaks at 3410.11 cm^{-1} and 3366.92 cm^{-1}, attributed to the stretching vibrations of the OH and NH groups, and at 2922.31 cm^{-1}, related to the stretching vibrations of the CH_2 CH_3 group. The peak at 2368.55 cm^{-1} corresponds to the stretching vibrations of C=O, indicating the presence of carbon dioxide or another potential molecule with this functional group in the tested sample.[44]

Two peaks, one at 1737.12 cm^{-1}, which is related to the stretching COOH groups,[45] and the other at 1620.43 cm^{-1}, which is related to the presence of C=C stretching vibrations in the aliphatic double bond or C=O stretching vibrations in an amide or ester functional group in the CD structure, respectively, are observed. The peak in the range of 1456 cm^{-1} often indicates the presence of a scissoring vibration of a methylene group (–CH_2) or aromatic C–C stretching. The presence of a peak at 1440 cm^{-1} is essentially due to the C–H bending vibrations in alkanes and that at 1387.11 cm^{-1} is related to the OH bending group, phenol. The peak at 1037.67 cm^{-1} is related to the C–O stretching vibrations in alkyl aryl ether and a peak at 760.22 cm^{-1} is related to cyclic C–H groups in the structure of CD aromatic hydrocarbons.[46] The peak at 620.22 cm^{-1} belongs to the halide group, since the CDs were synthesized from the natural precursor of the plant extract. The presence of these halide groups in CDs is inevitable as confirmed by CD spectroscopy.[47] On the other hand, the presence of NH and OH groups in the CDs confirms their solubility in water.

The FTIR spectrum of CD@AgNPs was analysed and compared with the spectrum of CDs (Fig. 3f). It can be seen that the spectrum of CD@AgNPs shows longer bands, with the presence of common peaks at 2368 cm^{-1} indicating the presence of carbon dioxide in the tested sample, which comes from atmospheric CO_2 present in the spectrometer environment; the sample itself may be contaminated with CO_2 either from the environment or during preparation.[48] The peaks at 1623.67 cm^{-1} and 1620.71 cm^{-1} can indicate the presence of C=C stretching vibrations in the aliphatic double bond or C=O stretching vibrations in an amide or ester functional group. The peak at 1456.13 cm^{-1} was caused by the bending shear vibration of the methylene groups and could be due to the presence of saturated hydrocarbons in the hybrid structure of CD@AgNPs. The peaks around 1245.16 cm^{-1} with varying relative intensities are related to the C–OH bending vibrations in the carboxylic acid and cyclic phenol groups and the C–O stretching vibrations.[49] Also, the stretching vibration at

1371.81 cm^{-1} in the spectrum of CD@AgNPs is related to the stretching vibration of CN in its bond with $AgNO_3$. The appearance of several sharp features in the range of 825.37 cm^{-1}, 800.02 cm^{-1}, 729.44 cm^{-1}, and 596.33 cm^{-1} is related to the interaction between AgNPs and oxygen-containing functional groups (C=O, C–OH and C–OOH), which confirms the electrostatic interaction of silver with CDs.

3.3. Optimizing the parameters in the assembly of CD@AgNPs

In order to detect and quantify the amount of cholesterol (Cho) and glucose (Glu) by CD@AgNPs, CD@AgNPs should be in the quenched state. Therefore, the volume of $AgNO_3$ solution and reaction time in the synthesis of CD@AgNPs were optimized.

Different volumes of $AgNO_3$ solution (20 mM, 200 to 1000 μL) were added to the carbon dot solution (60 μg mL^{-1}), where a volume ratio of Ag^+ : CD = 1 : 4 was kept in all tests. The UV-visible and fluorescence spectra were recorded for each sample to monitor the synthesis of AgNPs on CDs and its effect on the optical properties of the hybrid. As can be seen in Fig. 4a, the peak at 414 nm becomes more visible and intense by increasing the volume of $AgNO_3$. These peaks are due to localised surface plasmon resonance in AgNPs and clearly indicate the synthesis of AgNPs in the presence of CDs. Indeed, the functional groups on the surface of CDs act as reducing agents and result in the formation of AgNPs. The strongest peak with a blue shift compared to other samples was observed for the sample containing 1000 μL of $AgNO_3$ (20 mM), which indicates the formation of smaller AgNPs on CDs. In Fig. S3a,† the downward trend of the maximum LSPR peak (λ_{max}) as a function of the volume of $AgNO_3$ has been shown. It was found that increasing the Ag^+ : CD ratio led to a blue shift in λ_{max}, finally reaching 412 nm. This indicates that with the increase of $AgNO_3$ volume, the nucleation process and the stability of cluster distribution are more favorable and nanoparticles with smaller sizes are formed in the CD@AgNPs. The analysis of the relative fluorescence intensity of the same samples (F/F_0) shows stronger quenching with an increase in the Ag^+ : CD ratio (Fig. 4b). Since AgNPs act as acceptors, the presence of more acceptors at higher Ag^+ : CD ratios would lead to stronger FRET, and in turn, stronger fluorescence quenching in the CD@AgNP hybrid.

Since time is a very important parameter in the synthesis of CD@AgNPs, the absorption and fluorescence of the synthesized sample were monitored by adding 1000 μL $AgNO_3$ (20 mM) to the CDs at time intervals of 0 to 30 minutes. Fig. 4c shows the extinction spectrum of Cd@AgNP during the synthesis. The intensity of the localized surface plasmon resonance peak (λ_{max}) increased over time, showing the formation and growth of AgNPs (Fig. S3b†). The formation of AgNPs is evidenced by strong fluorescence quenching through the FRET mechanism (Fig. 4d), indicating that silver nanoparticles are well formed in the structure of CD@AgNPs through electrostatic interactions with CDs.
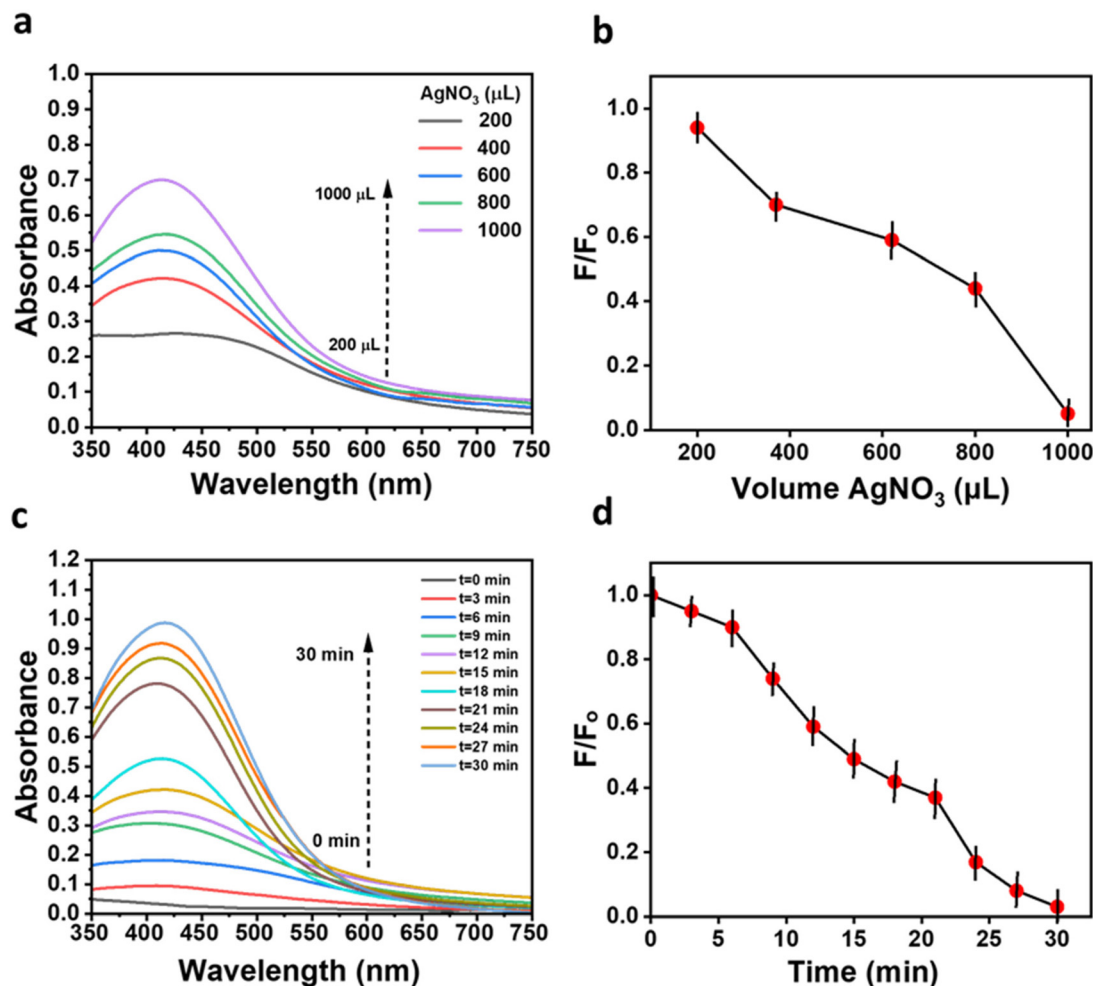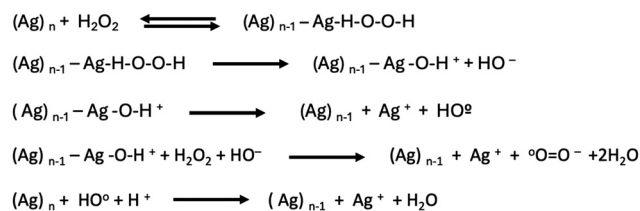
Fig. 4 (a) Extinction spectrum and (b) the relative fluorescence intensity of the CD@AgNP hybrid sample as a function of different volumes of AgNO$_3$ (200 400, 600 800, and 1000 μL). (c) Time evolution of the UV-visible spectrum and (d) the relative fluorescence intensity of the CD@AgNP hybrid. 1000 μL of AgNO$_3$ (20 mM) and the Ag$^+$: CD volume ratio of 1 : 4 were used for the synthesis. Standard deviations are for three replicates. λ_{ex} = 350 nm and λ_{em} = 409 nm were used in fluorescence studies.

3.4. Fluorescence recovery assessment

To assess whether the fluorescence of CDs could be recovered by etching AgNPs, H$_2$O$_2$ was used as a strong oxidizing agent. It is expected that Ag^0 is oxidized to Ag$^+$ and leads to the recovery of CD fluorescence (λ_{em} = 409 nm) under λ_{ex} = 350 nm.

Indirect measurement of cholesterol and glucose levels was carried out through the oxidation of these molecules by ChOx and GOx enzymes and the production of the H$_2$O$_2$ by-product. H$_2$O$_2$ undergoes a Fenton-like reaction with AgNPs that produces highly reactive oxygen species (ROS) and causes oxidative dissolution of AgNPs to Ag$^+$ ions[50]. The oxidative dissolution of AgNPs in the CD@AgNP hybrid structure is proportional to the amount of produced H$_2$O$_2$. It should be noted that ROS, including free hydroxyl and hydroxyl radicals bound to the silver metal, lead to the formation of superoxide radicals and hydroperoxyl radicals that are the main active species in the dissolution of silver nanoparticle catalysts[51]. Scheme 1 shows the mechanism of this oxidative dissolution process by

$$(Ag)_n + H_2O_2 \rightleftharpoons (Ag)_{n-1} - Ag\text{-}H\text{-}O\text{-}O\text{-}H$$

$$(Ag)_{n-1} - Ag\text{-}H\text{-}O\text{-}O\text{-}H \longrightarrow (Ag)_{n-1} - Ag\text{-}O\text{-}H^+ + HO^-$$

$$(Ag)_{n-1} - Ag\text{-}O\text{-}H^+ \longrightarrow (Ag)_{n-1} + Ag^+ + HO^\circ$$

$$(Ag)_{n-1} - Ag\text{-}O\text{-}H^+ + H_2O_2 + HO^- \longrightarrow (Ag)_{n-1} + Ag^+ + {}^\circ O{=}O^- + 2H_2O$$

$$(Ag)_n + HO^\circ + H^+ \longrightarrow (Ag)_{n-1} + Ag^+ + H_2O$$

Scheme 1 Catalytic reaction of silver nanoparticles with hydrogen peroxide.

H$_2$O$_2$.[52] As shown in Fig. 5a (inset image), the oxidative dissolution of AgNPs changes the color of the solution from yellowish brown to colorless as a result of etching with increasing H$_2$O$_2$ concentration, showing the potential for designing a naked-eye colorimetric biosensor using this method. On the other hand, it was found that the fluorescence of the sample is recovered by adding more H$_2$O$_2$.
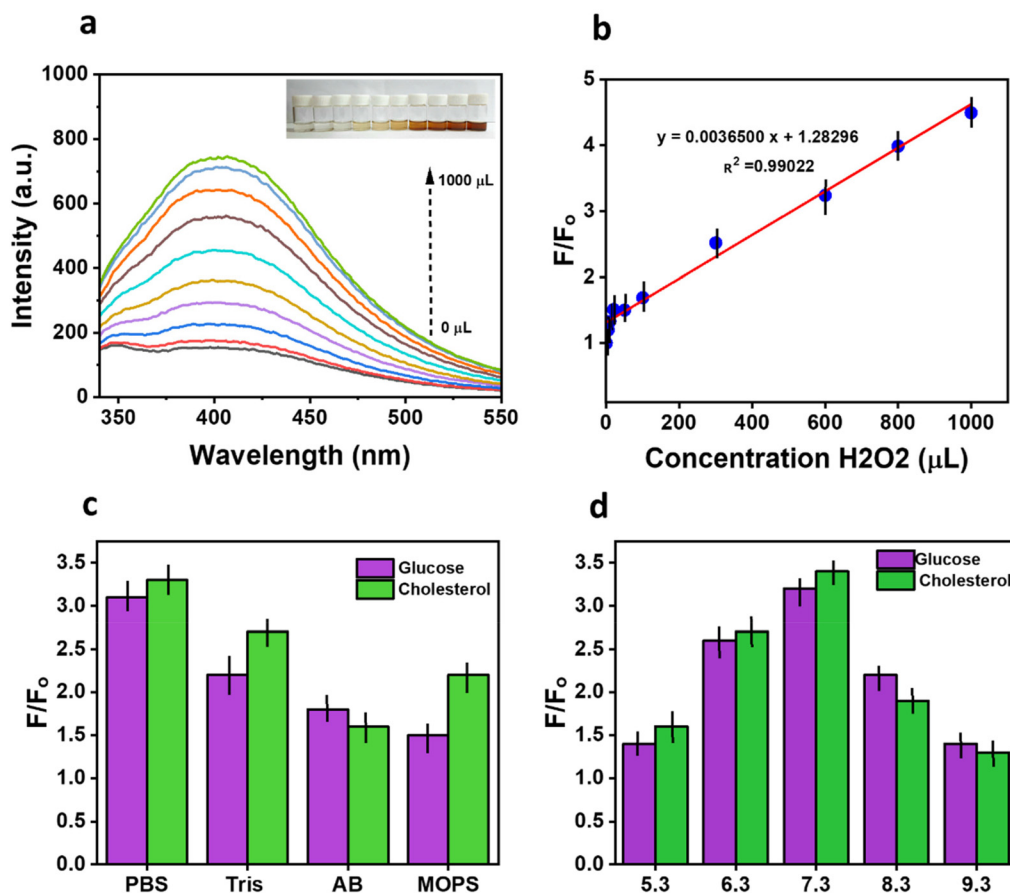
Fig. 5 (a) Change in the fluorescence emission of CD@AgNPs in the presence of varying concentrations of H_2O_2. (b) Change in the F to F_0 ratio in the CD@AgNP hybrid with different concentrations of H_2O_2 (0–1000 μM). (c) Change in the F to F_0 ratio in the CD@AgNP hybrid in the presence of H_2O_2 and different buffers (Tris, AB, MOPS, and PBS) at 5 mM concentration. (d) Relative fluorescence (F/F_0) in the CD@AgNP hybrid in the presence of H_2O_2, and phosphate buffered saline (PBS) at pH = 5.3, 6.3, 7.3, 8.3, and 9.3 and 5 mM concentration were used in all experiments. ChOx (1 mg mL^{-1}), Ch (250 μM), GOx (1 mg mL^{-1}), and Glu (60 μM) as well as λ_{ex} = 350 nm and λ_{em} = 409 nm were used in these experiments.

It was also found in Fig. 5b that the fluorescence was recovered linearly with an increase in the H_2O_2 concentration (F/F_0 = (3.6500×10^{-3}) $[H_2O_2]$ + 1.282 and R^2 = 0.9902) with a limit of detection of 6.36 μM (*i.e.*, LOD = $3\sigma_{blank}$/slope, where σ_{blank} is the standard deviation of the blank samples, with a relative standard deviation of RSD less than 5%), as higher concentrations of H_2O_2 led to stronger etching of AgNPs, and in turn, the fluorescence recovery was evidenced by the change in the color of the solution from brown yellow to colorless.

The activity of enzymes might be affected by the pH of the reaction. Therefore, we considered the type of buffer and pH as important factors that might affect the kinetics of H_2O_2 production as well as its stability in the environment. For this purpose, the buffer medium and the pH of the Cho and Glu enzymatic reaction were optimized. Four buffers were selected and prepared, including Tris buffer (5 mM and pH = 7), acetate buffer (AB, 5 mM, pH = 7), 3-(N-morpholino)propane sulfonic acid buffer (MOPS, 5 mM and pH-7-M), and phosphate buffered saline (PBS, 5 mM and pH = 7). Different concentrations of cholesterol and glucose were prepared in the presence of ChOx and GOx enzymes in each of these buffers.

After 30 minutes of incubation, leading to the reaction of cholesterol and glucose with the corresponding enzymes and the production of H_2O_2, 500 μL of CD@AgNPs was added and the fluorescence emission ratio in each of the buffer environments was recorded to perform the reaction and produce H_2O_2 and destroy AgNPs. As can be seen in Fig. 5c, the results showed the best fluorescence ratio from the reaction of ChOx and GOx enzymes with Cho and Glu in phosphate buffered saline (PBS). Then, PBS was prepared at different pH values (pH = 5.3, 6.3, 7.3, 8.3, and 9.3). The enzyme reaction environment at pH = 7.3, neutral and stable pH, led to the highest fluorescence emission ratio (Fig. 5d). Therefore, PBS with pH = 7.3 was selected as the optimal buffer and pH for further studies.

The catalytic activity of GOx decreases in the reaction with Glo in a basic pH environment, and this has been attributed to the protonation of the active site histidine in the flavin adenine dinucleotide (FAD) molecule in GOx, *i.e.*, the protonated histidine leads to a decrease in the kinetic barrier for electron transfer to oxygen. But at neutral pH, the polarizability decreases, which reduces the inherent charge barrier, and

in this environment, the catalytic activity of GOx with Glo is carried out optimally. Also, in the ChOx enzyme, with increasing pH, the charge on one or all of the amino acids in the ChOx enzyme is such that Cho can neither be properly bound nor react properly to produce 4-cholesten-3-one.[53] But at pH = 7.3, due to structural changes in the enzyme configuration, the ionizable groups located at the active sites of the enzyme decreased, and the enzyme reacted optimally with Cho, and at pH = 7.3, the enzyme activity was more stable.[54,55]

3.5. Determination of glucose and cholesterol in complex biological samples

Maintaining the concentrations of cholesterol (Cho) and glucose (Glu) in the optimal range is very important for human health. Therefore, Cho and Glu are vital biomarkers for clinical diagnosis and health management. The cholesterol oxidase (ChOx) and glucose oxidase (GOx) enzymes could interact with these molecules and produce H_2O_2 as a by-product. The produced H_2O_2 is an intermediate identifier in the reaction that could etch the AgNPs in CD@AgNPs hybrid, leading to fluorescence recovery. Therefore, a combination of the CD@AgNP hybrid and the aforementioned oxidase enzymes could be used as an off–on fluorescent probe for the detection and quantification of cholesterol and glucose as important biological biomarkers. Fig. 6a and b show the schematic of the enzymatic reaction of Cho and Glu with oxidases and the production of H_2O_2 and the indirect detection of Cho and Glu with the CD@AgNP hybrid.

To detect and quantify Cho and Glu, PBS at a pH of 7.3 was used. The fluorescence recovery was measured after 30 min, allowing the reaction to complete. The oxidase enzymes were used at 1 mg mL^{-1} in phosphate buffer, where the concentrations of cholesterol (2–60 μM) and glucose (4–250 μM) were varied in different experiments. In both cases, the fluorescence intensity was recovered by increasing the concentration of the analyte (Fig. 6c and d), evidenced by color changes proportional to the concentrations of the analyte. The analysis of these results revealed that the fluorescence intensity has a linear relationship with the concentrations of the analyte. In particular, for cholesterol, the LOD was 3 μM ($F/F_0 = (4.0960 \times 10^{-2})$ [H_2O_2] + 1.2185 and $R^2 = 0.9939$) and for glucose, the LOD was 38 μM ($F/F_0 = (1.0744 \times 10^{-2})$ [H_2O_2] + 1.34017 and $R^2 = 0.9879$). These LOD values were favorably lower than the amount of cholesterol (>2.7 mM) and glucose (2.8 mM) in the plasma sample of a healthy person.[56,57]

To investigate whether a complex medium affects the sensitivity and selectivity of the designed biosensors, we employed artificial human plasma fluid to mimic the human plasma. We first spiked glucose and cholesterol into the medium and then quantified the amount of cholesterol and glucose in the samples using the obtained calibration curves. Fig. 6e–f show that the sample is well matched with the calibration curve, where the percentage of recovery for glucose and cholesterol has less than 5% error compared with the spiked concentrations (Table S1†).

The results indicated that the CD@AgNP hybrid biosensor could be successfully used for the detection and quantification of cholesterol and glucose in a complex medium (Fig. 6e and f). In addition to the excellent sensitivity and selectivity, the optimal LODs obtained in the designed biosensor were compared to other works (Table S2†), indicating the potential applications of the CD@AgNP hybrid biosensor in the field of medicine owing to its simplicity, low cost and accuracy for the detection and quantification of two important biomarkers in human body fluids.

In order to evaluate the selectivity of the designed turn-on probe, the fluorescence recovery of CD@AgNPs was investigated in the presence of potential interfering substances such as maltose, fructose, saccharide and lactose, xylose, glutamic acid, and lysine, and ions such as Na$^+$ and K$^+$. It was found that interfering substances with a 10× concentration of glucose and cholesterol had no significant effect on fluorescence recovery. On the other hand, the color of the solution changed from yellowish brown to colorless when the probe was exposed to only glucose or cholesterol. The selectivity results are summarized in Fig. S4a and b,† which indicate that the assay is not only highly sensitive but also exhibits excellent selectivity towards glucose and cholesterol.

4. Conclusion

This study investigated the potential of a carbon dot@silver nanoparticle hybrid system as a turn-on fluorescent probe for the detection and quantification of two important biomarkers (glucose and cholesterol). The green-synthesized CDs showed excitation-dependent fluorescence, which is common in carbon dots. Additionally, CDs possessed a surface chemistry rich in negatively charged functional groups that provide a suitable opportunity for the interaction between CDs and Ag$^+$ ions, leading to the nucleation and growth of AgNPs on the surface of CDs. This nanohybrid synthesis approach has several advantages over other methods. First, the CDs were prepared alone and without adding any chemicals from *Oliveria decumbens* Vent. plant extract in a short time using a microwave, and the CD@AgNP system was prepared in the vicinity of the Ag$^+$ solution without using expensive equipment and using water as a solvent at room temperature. The UV-visible spectrum of CD@AgNPs compared to citrate-AgNPs and a mixture of citrate-AgNPs and CDs showed a red shift, indicating the reduction of Ag$^+$ by CD and the formation of AgNPs with the characteristic localised surface plasmon resonance of AgNPs and the yellowish brown color. The fluorescence emission of CDs was effectively quenched with the growth of AgNPs, which can be attributed to the FRET mechanism and charge transfer from excited CDs (donor) to AgNPs (acceptor). On the other hand, the CD@AgNP hybrid recovered its fluorescence remarkably in the presence of different concentrations of H_2O_2, where hydrogen peroxide acted as an etching agent for AgNPs. Based on this concept, the CD@AgNP hybrid was employed to indirectly detect glucose and cholesterol because H_2O_2 is the
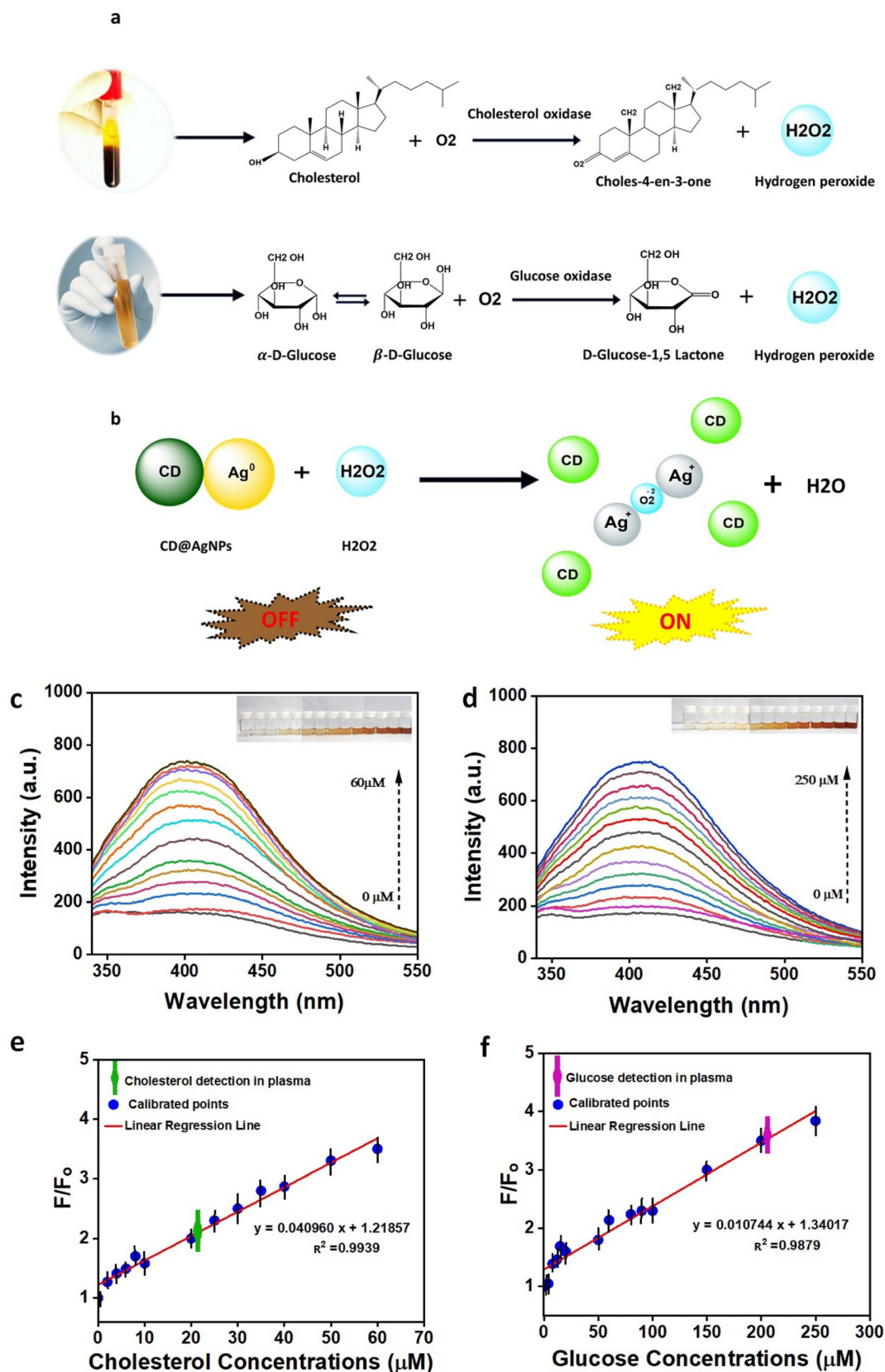
Fig. 6 (a) Schematic detection of cholesterol and glucose based on the enzymatic reaction-assisted approach and (b) etching of AgNPs in the CD@AgNP hybrid. Changes in the fluorescence spectrum as a function of (c) cholesterol (2–60 μM) and (d) glucose (4–250 μM) concentration and the corresponding calibration curves for (e) cholesterol and (f) glucose. The conditions are the same for all samples.

by-product of the enzymatic reaction of cholesterol/glucose oxidase enzymes with cholesterol and glucose. The obtained results are in the linear range of 2–60 μM for identifying cholesterol with a LOD = 3.0 μM and R^2 = 0.9939 and also a linear range of 4–250 μM for glucose with a LOD = 38 μM and R^2 = 0.9879, which are much less than the values reported in the literature (Table S2†). Molecular detection systems such as electrochemical, optical, thermometric, piezoelectric and magnetic systems, among which molecular biosensors are mainly electrochemical, have relatively high selectivity for glucose, and are also inexpensive and resistant to pH, ionic strength and temperature, which allows them to be used under a variety of conditions during the manufacturing process.[58–60] However, there are several problems, especially regarding the distorted responses, unpredictable signal transfer *in vivo* that requires frequent calibration against fingerstick samples, complex equipment, sample pretreatment, *etc*.[61] Meanwhile, fluorescence-based systems with hybrid nanoparticles with fluorescent materials have been used for glucose and cholesterol detection, which have attracted increasing attention.[62] In this study, we present a biosensor in the aqueous state of CD@AgNPs, which has advantages over solid-state sensors used in electrochemical applications, such as high sensitivity, little or no damage to the host system, the ability to use time-resolved fluorescence and investigate the structure and distribution of biomolecules by various phenomena, fluorescence resonance energy transfer (FRET) and light-induced electron transfer.[63] Typically, the off–on state caused by H_2O_2 produced by the enzymatic reaction of GOx and ChOx with glucose and cholesterol can cause the fluorescence of CDs to turn on and the oxidation of silver nanoparticles, with the degree of turn-on indicating the amount of glucose and cholesterol.[64] This strategy with the high sensitivity and selectivity of the CD@AgNP hybrid in the detection and quantification of cholesterol and glucose in body fluids (artificial human plasma) could open new avenues for designing similar biosensors for various biomedical and environmental applications.

Data availability

The authors will provide the data upon request.

Conflicts of interest

There are no conflicts to declare.

References

1 S. Rahmati-Ahmadabad, *et al.*, Effects of exercise on reverse cholesterol transport: A systemized narrative review of animal studies, *Life Sci.*, 2019, **224**, 139–148.

2 M. C. Gray, *et al.*, Microenzymatic fluorescence assay for serum cholesterol, *Anal. Biochem.*, 1995, **224**(1), 286–292.

3 D. C. Rule, M. Liebman and Y. B. Liang, Impact of different dietary fatty acids on plasma and liver lipids is influenced by dietary cholesterol in rats, *J. Nutr. Biochem.*, 1996, **7**(3), 142–149.

4 T. Lin, *et al.*, A sensitive colorimetric assay for cholesterol based on the peroxidase-like activity of MoS 2 nanosheets, *Microchim. Acta*, 2017, **184**, 1233–1237.

5 Y. Huang, *et al.*, Graphene and Au NPs co-mediated enzymatic silver deposition for the ultrasensitive electrochemical detection of cholesterol, *Biosens. Bioelectron.*, 2018, **102**, 560–567.

6 B. Thorens, Neuronal glucose sensing mechanisms and circuits in the control of insulin and glucagon secretion, *Physiol. Rev.*, 2024, **104**, 1461–1486.

7 C. Liu, *et al.*, Association of the triglyceride glucose index with all cause and CVD mortality in the adults with diabetes aged< 65 years without cardiovascular disease, *Sci. Rep.*, 2025, **15**(1), 2745.

8 A. Chandramouli and S. S. Kamat, A facile LC-MS method for profiling cholesterol and cholesteryl esters in mammalian cells and tissues, *Biochemistry*, 2024, **63**(18), 2300–2309.

9 M. MacAulay, *et al.*, Continuous-flow enzymatic determination of total serum cholesterol and method standardization with CDC-calibrated pooled sera, *Clin. Chem.*, 1980, **26**(7), 896–902.

10 L. L. Abell, *et al.*, *A simplified method for the estimation of total cholesterol in serum and demonstration of its specificity*, 1952.

11 I. W. Duncan, A. Mather and G. R. Cooper, *The procedure for the proposed cholesterol reference method*. 1982: Clinical Chemistry Division, Center for Environmental Health, Centers for ....

12 S.-M. Wang, *et al.*, Single-particle detection of cholesterol based on the host-guest recognition induced plasmon resonance energy transfer, *Chin. Chem. Lett.*, 2023, **34**(7), 108053.

13 B. Kumar and S. K. Sinha, Development of a highly sensitive non-enzymatic electrochemical cholesterol biosensor based on Ag with Cu2O nanomaterial deposited on TiO2 nanotubes, *Measurement*, 2024, **232**, 114707.

14 J. Wei, *et al.*, Targeted bile acids metabolomics in cholesterol gallbladder polyps and gallstones: From analytical method development towards application to clinical samples, *J. Pharm. Anal.*, 2023, **13**(9), 1080–1087.

15 R. Ahmad, N. Tripathy and Y.-B. Hahn, High-performance cholesterol sensor based on the solution-gated field effect transistor fabricated with ZnO nanorods, *Biosens. Bioelectron.*, 2013, **45**, 281–286.

16 S. Zhang, *et al.*, Synergistic Co-Assembly of Natural Oxidase and Peptide-Heme Nanozyme for In Situ H_2O_2 Removal with Enhanced Catalytic Efficiency and Stability, *Nano Lett.*, 2024, **24**(48), 15371–15378.

17 I. Zare, *et al.*, Modulating the catalytic activities of nanozymes for molecular sensing, *Nano Today*, 2024, **56**, 102276.

18 H. V. Xu, Y. Zhao and Y. N. Tan, Nanodot-directed formation of plasmonic-fluorescent nanohybrids toward dual optical detection of glucose and cholesterol via hydrogen peroxide sensing, *ACS Appl. Mater. Interfaces*, 2019, **11**(30), 27233–27242.

19 B. Kumara, P. Kalimuthu and K. Prasad, Synthesis, properties and potential applications of photoluminescent carbon nanoparticles: A review, *Anal. Chim. Acta*, 2023, **1268**, 341430.

20 M. Tavakkoli Yaraki, *et al.*, Nanosilver-enhanced AIE photosensitizer for simultaneous bioimaging and photodynamic therapy, *Mater. Chem. Front.*, 2020, **4**(10), 3074–3085.

21 M. Tavakkoli Yaraki, *et al.*, Metal-enhancement study of dual functional photosensitizers with aggregation-induced emission and singlet oxygen generation, *Nanoscale Adv.*, 2020, **2**(7), 2859–2869.

22 J. Xue, *et al.*, Etching Triangular Silver Nanoparticles by Self-generated Hydrogen Peroxide to Initiate the Response of an Electrochemiluminescence Sensing Platform, *Anal. Chem.*, 2020, **92**(20), 14203–14209.

23 H. Liu, *et al.*, A review of carbon dots in synthesis strategy, *Coord. Chem. Rev.*, 2024, **498**, 215468.

24 S. Daniel, *Characterization of carbon dots, in Carbon Dots in Analytical Chemistry*, Elsevier, 2023. p. 43–58.

25 B. Lee, *et al.*, Automated approach to in vitro image-guided photothermal therapy with top-down and bottom-up-synthesized graphene quantum dots, *Nanomaterials*, 2023, **13**(5), 805.

26 X. Chu, *et al.*, The acetone sensing properties of ZnFe2O4-graphene quantum dots (GQDs) nanocomposites at room temperature, *Phys. E*, 2019, **106**, 326–333.

27 Y. Dong, *et al.*, Blue luminescent graphene quantum dots and graphene oxide prepared by tuning the carbonization degree of citric acid, *Carbon*, 2012, **50**(12), 4738–4743.

28 G. Amin, *et al.*, Essential oil composition and antimicrobial activity of Oliveria decumbens, *Fitoterapia*, 2005, **76**(7–8), 704–707.

29 S. E. Sajjadi and S. A. Hoseini, Essential oil constituents of Oliveria decumbens Vent, *J. Essent. Oil Res.*, 2002, **14**(3), 220–221.

30 X. Li, *et al.*, Engineering surface states of carbon dots to achieve controllable luminescence for solid-luminescent composites and sensitive Be2 + detection, *Sci. Rep.*, 2014, **4**(1), 4976.

31 P. Singh, *et al.*, Assessment of biomass-derived carbon dots as highly sensitive and selective templates for the sensing of hazardous ions, *Nanoscale*, 2023, **15**(40), 16241–16267.

32 M. Sudolska, *et al.*, Nature of absorption bands in oxygen-functionalized graphitic carbon dots, *J. Phys. Chem. C*, 2015, **119**(23), 13369–13373.

33 R. E. Ambrusi, *et al.*, Density functional theory model for carbon dot surfaces and their interaction with silver nanoparticles, *Phys. E*, 2019, **114**, 113640.

34 J. Jiménez-López, *et al.*, Graphene quantum dots-silver nanoparticles as a novel sensitive and selective lumine-scence probe for the detection of glyphosate in food samples, *Talanta*, 2020, **207**, 120344.

35 P. Reineck, *et al.*, Distance and wavelength dependent quenching of molecular fluorescence by Au@ SiO$_2$ core–shell nanoparticles, *ACS Nano*, 2013, **7**(8), 6636–6648.

36 R. Kato, *et al.*, Highly stable polymer coating on silver nanoparticles for efficient plasmonic enhancement of fluorescence, *ACS Omega*, 2022, **7**(5), 4286–4292.

37 Z. Zhelev, H. Ohba and R. Bakalova, Single quantum dot-micelles coated with silica shell as potentially non-cytotoxic fluorescent cell tracers, *J. Am. Chem. Soc.*, 2006, **128**(19), 6324–6325.

38 Y. Chen, *et al.*, A self–quenching–resistant carbon–dot powder with tunable solid–state fluorescence and construction of dual–fluorescence morphologies for white light–emission, *Adv. Mater.*, 2016, (2), 312–318.

39 H. Abdolmohammad-Zadeh, Z. Azari and E. Pourbasheer, Fluorescence resonance energy transfer between carbon quantum dots and silver nanoparticles: Application to mercuric ion sensing, *Spectrochim. Acta, Part A*, 2021, **245**, 118924.

40 M. Amjadi, Z. Abolghasemi-Fakhri and T. Hallaj, Carbon dots-silver nanoparticles fluorescence resonance energy transfer system as a novel turn-on fluorescent probe for selective determination of cysteine, *J. Photochem. Photobiol., A*, 2015, **309**, 8–14.

41 J. M. Arroyave, Experimental and DFT Studies of Hybrid Silver/Cdots, *Nanoparticles*, 2020, **124**, 2425–2435.

42 Q. Xu, *et al.*, Synthesis, mechanical investigation, and application of nitrogen and phosphorus co-doped carbon dots with a high photoluminescent quantum yield, *Nano Res.*, 2018, **11**, 3691–3701.

43 T. Liu, *et al.*, Silver nanoparticle@ carbon quantum dot composite as an antibacterial agent, *RSC Adv.*, 2022, **12**(16), 9621–9627.

44 E. Mathez, *et al.*, The determination of the O content of diamond by microactivation, *Am. Mineral.*, 1993, **78**(7–8), 753–761.

45 M. A. Aldosari, A. A. Othman and E. H. Alsharaeh, Synthesis and characterization of the in situ bulk polymerization of PMMA containing graphene sheets using microwave irradiation, *Molecules*, 2013, **18**(3), 3152–3167.

46 B. De and N. Karak, A green and facile approach for the synthesis of water soluble fluorescent carbon dots from banana juice, *RSC Adv.*, 2013, **3**(22), 8286–8290.

47 G. A. Ali, *et al.*, One-step electrochemical synthesis of MoS 2/graphene composite for supercapacitor application, *J. Solid State Electrochem.*, 2020, **24**, 25–34.

48 V. Țucureanu, A. Matei and A. M. Avram, FTIR spectroscopy for carbon family study, *Crit. Rev. Anal. Chem.*, 2016, **46**(6), 502–520.

49 K. Hola, *et al.*, Graphitic nitrogen triggers red fluorescence in carbon dots, *ACS Nano*, 2017, **11**(12), 12402–12410.

50 W. He, *et al.*, Mechanisms of the pH dependent generation of hydroxyl radicals and oxygen induced by Ag nanoparticles, *Biomaterials*, 2012, **33**(30), 7547–7555.

51 D. He, J. J. Dorantes-Aranda and T. D. Waite, Silver Nanoparticle Algae Interactions: Oxidative Dissolution, Reactive Oxygen Species Generation and Synergistic Toxic Effects, *Environ. Sci. Technol.*, 2012, **46**(16), 8731–8738.

52 A. B. Albeladi, S. A. Al-Thabaiti and Z. Khan, Effect of CTAB on the surface resonance plasmon intensity of silver nanoparticles: Stability and oxidative dissolution, *J. Mol. Liq.*, 2020, **302**, 112565.

53 Y. Kang, A. G. Marangoni and R. Y. Yada, Effect Of Two Polar Organic–Aqueous Solvent Systems On The Structure–Function Relationships Of Proteases III. Papain And Trypsin, *J. Food Biochem.*, 1993, **17**(6), 389–405.

54 J. Kinsella, *Principles of Enzymology for the Food Sciences/Principles of Enzymology for the Food Sciences*, John R. Whitaker, Marcel Dekker Inc., Elsevier, New York (1972), 1973, vol. 636 pp. $26.

55 M. Heinelt, T. Nöll and G. Nöll, Spectroelectrochemical Investigation of Cholesterol Oxidase from Streptomyces lividans at Different pH Values, *ChemElectroChem*, 2019, **6**(8), 2174–2181.

56 L. Ding, *et al.*, Dual-mode cholesterol sensor based on gold nanorods and carbon quantum dots, *Mater. Chem. Phys.*, 2023, **309**, 128336.

57 Z. Zhang, *et al.*, Highly sensitive on-site detection of glucose in human urine with naked eye based on enzymatic-like reaction mediated etching of gold nanorods, *Biosens. Bioelectron.*, 2017, **89**, 932–936.

58 L. C. Clark Jr and C. Lyons, Electrode systems for continuous monitoring in cardiovascular surgery, *Ann. N. Y. Acad. Sci.*, 1962, **102**, 29–45.

59 I. Satoh, I. Karube and S. Suzuki, Enzyme electrode for sucrose, *Biotechnol. Bioeng.*, 1976, **18**(2), 269–272.

60 A. Hiratsuka, K. Fujisawa and H. Muguruma, Amperometric biosensor based on glucose dehydrogenase and plasma-polymerized thin films, *Anal. Sci.*, 2008, **24**(4), 483–486.

61 J. P. Chambers, *et al.*, Biosensor recognition elements, *Curr. Issues Mol. Biol.*, 2008, **10**(1–2), 1–12.

62 L. Chen, E. Hwang and J. Zhang, Fluorescent nanobiosensors for sensing glucose, *Sensors*, 2018, **18**(5), 1440.

63 A. Hoque, *et al.*, *Carbon dots assembly on metal nanostructures for sensing applications in environmental analysis*, in *Nanomaterials in Environmental Analysis*, Elsevier, 2024, pp. 537–564.

64 J.-L. Ma, *et al.*, Simple and cost-effective glucose detection based on carbon nanodots supported on silver nanoparticles, *Anal. Chem.*, 2017, **89**(2), 1323–1328.